Physics of Plasmas ARTICLE scitation.org/journal/php

Electrostatic quasi-neutral formulation of global cross-separatrix particle simulation in field-reversed configuration geometry

Cite as: Phys. Plasmas **27**, 082504 (2020); doi: 10.1063/5.0012439
Submitted: 30 April 2020 · Accepted: 14 July 2020 ·
Published Online: 4 August 2020

C. K. Lau,[1,a)] D. P. Fulton,[1] J. Bao,[2] Z. Lin,[2] S. Dettrick,[1] M. Binderbauer,[1] T. Tajima,[1,2] and L. Schmitz[1,3]

AFFILIATIONS

[1]TAE Technologies, Inc., Foothill Ranch, California 92610, USA
[2]Department of Physics and Astronomy, University of California, Irvine, California 92697, USA
[3]Department of Physics and Astronomy, University of California, Los Angeles, California 90095, USA

Note: This paper is part of the Special Collection: Building the Bridge to Exascale Computing: Applications and Opportunities for Plasma Science

[a)]**Author to whom correspondence should be addressed:** clau@tae.com

ABSTRACT

A quasi-neutral blended drift-Lorentz particle model of the field-reversed configuration (FRC) has been developed and implemented in the particle-in-cell code named ANC. A field-aligned mesh and corresponding mesh operations are constructed for solving self-consistent electric fields in FRC geometry. Particle dynamics are described in cylindrical coordinates to allow for cross-separatrix simulation coupling the core and scrape-off layer regions of the FRC. This new model is successfully verified against analytically derived dispersion relations, and FRC turbulence is studied using the blended model for the first time.

I. INTRODUCTION

An ideal field-reversed configuration (FRC) is a compact toroid (CT) with purely poloidal magnetic fields. It consists of two regions separated by a separatrix: an inner, closed field-line core region and an outer, open field-line scrape-off layer (SOL) region. The FRC concept as a fusion reactor has several benefits: (1) β (the ratio of plasma pressure to magnetic energy density) near unity suggests more economical magnetic energy costs; (2) compact shape simplifies the device hull and external magnetic field coils; (3) SOL may be connected to the divertor arbitrarily far from the FRC core; and (4) the lack of toroidal magnetic fields radically changes the magnetic topology and the consequential stability of the plasma.

In the C2/C2U FRC experiments at TAE Technologies, Doppler backscattering (DBS)[1] measurements of density fluctuations showed distinct qualities between the core and SOL. In the SOL, the fluctuation spectrum is highest in amplitude at ion-scale wavenumbers, decreasing exponentially toward electron-scale wavenumbers. In the core, fluctuations are overall lower in amplitude relative to the SOL, and the highest amplitude fluctuations are located at electron-scale wavenumbers.[2]

Early efforts to understand this phenomenon in the FRC used linear GTC [the Fortran based gyrokinetic (GK) toroidal code[3]] simulations localized to drift-surfaces using gyrokinetic particles.[4] Within gyrokinetically valid parameters ($\langle \rho_i/L_n \rangle < 1$), these simulations show the FRC core to be stable while various instabilities were able to arise at a range of toroidal wavenumbers and pressure profiles in the SOL.[5,6]

Although consistent with experiment, the localized linear GTC simulations were insufficient for turbulence simulations due to the coupled nature of the core and SOL. In order to address the coupled nature of the core and SOL regions, a new simulation model spanning across the separatrix has been developed. The formulation described in this paper is implemented as the particle-in-cell (PIC) code named "ANC." Closely related to and based on the parallelism of GTC, this code is written in Fortran and uses OpenMP/message passing interface (MPI) parallelization while updates for graphics processing unit (GPU) acceleration are in progress. Unlike the more "device agnostic"

GTC, the simulation code ANC is a microturbulence code tailored to investigate transport in FRC geometry using a first-principles model.

In follow-up non-local nonlinear ANC and GTC simulations using a gyrokinetic ion model with an adiabatic electron response, instability was shown to only grow in the SOL,[7–9] consistent with the local GTC results. These ANC simulations use a non-local simulation domain extending from the FRC core to the SOL within the confinement vessel with an axial periodic boundary condition. The non-local capability was shown to be important for allowing the fluctuations, which arise due to SOL instability, to non-linearly spread into the core, resulting in a fluctuation spectrum that is qualitatively consistent and quantitatively within expectations with experimental measurements.[2] As the next generation of high performance computers enters exascale computing regimes, algorithms and models can also be updated to accommodate more realistic physics. Because of the low magnetic fields, the gyrokinetic model is inadequate to fully describe the possible particle trajectories in the FRC,[10] such as Fig. 8 or betatron orbits. To overcome this, the blended particle model, described in Sec. III, is implemented in ANC. Furthermore, in order to calculate particle diffusivity and electron thermal conductivity, the non-adiabatic electron response must be represented. Using the blended model, the non-adiabatic electron response is now implemented, and it is now possible to self-consistently calculate electron transport from ANC simulations. At present, ANC is electrostatic and nonlinear, based on the Vlasov–Poisson system of equations. With the goal of understanding transport scaling applicable toward future reactor-grade plasmas, effective collisionality is assumed to be low and no collisional effects are present in the model. The particle model is generalized, allowing gyrokinetic (GK) or blended drift-Lorentz ("blended") particle species. Toward the goal of experimental validation, it accepts arbitrary numerical FRC equilibria, spanning closed and open magnetic field-line regions. In this paper, the formulation of the simulation model implemented in ANC is described: the equilibrium and coordinate system, including the field-aligned mesh, are presented in Sec. II; the blended and gyrokinetic particle models are described in Sec. III; Sec. IV is devoted to solving for the self-consistent fields; various benchmarks are discussed in Sec. V; and preliminary FRC simulation results are shown in Sec. VI.

II. EQUILIBRIUM AND COORDINATE SYSTEM

A. Equilibrium

ANC is built to use equilibrium data such as ψ_{pol}, n_e, n_i, T_e, and T_i on a 2D R-Z plane with quantities assumed to be azimuthally symmetric. Simulations use equilibria generated using the LReqMI code,[11] and experimentally relevant equilibria are obtained by comparing synthetic diagnostics with experimental results.

Currently, simulations are confined to a nonlocal domain spanning the confinement vessel region of the reactor with periodic boundaries in the axial directions and neglect parallel outflow effects. This assumption limits the model to investigations of perpendicular transport only. As shown in Fig. 1, the magnetic field null region is excluded in simulations using the gyrokinetic particle model to preserve gyrokinetic validity.

A true equilibrium distribution function is of the following form:

$$F_0(\tilde{\psi}, E) = \frac{n(\tilde{\psi})}{(2\pi T(\tilde{\psi})/m)^{3/2}} e^{-E/T(\tilde{\psi})}, \tag{1}$$

where $\tilde{\psi} \equiv \psi(R, Z) - \frac{mv_\zeta R}{q} = -P_\zeta/q$ is the modified poloidal flux function, which is a constant of motion due to its dependence on only the canonical angular momentum. Currently, equilibria generated by LReqMI are spatially dependent but not velocity dependent. While questionable for ions in the FRC, this function can be expanded with the assumption of $\psi(R, Z) \gg \frac{mv_\zeta R}{q}$, a necessary step to match currently available experimentally relevant pressure profiles,

$$\begin{aligned} F_0(\tilde{\psi}, E) &\approx f_0(\psi, E) + \frac{\partial f_0(\psi, E)}{\partial \psi}\left(-\frac{mv_\zeta R}{q}\right) + \cdots \\ &\approx f_0(\psi, E)\left(\alpha_0(v_\zeta^0) + \alpha_1(v_\zeta^1) + \cdots\right), \end{aligned} \tag{2}$$

where f_0 is an analytic distribution function dependent on only the spatially dependent ψ and the particle energy E. Taking f_0 to be a local Maxwellian with spatially dependent temperatures and densities,

$$f_M(\psi, E) = \frac{n(\psi)}{(2\pi T(\psi)/m)^{3/2}} e^{-E/T(\psi)}, \tag{3}$$

the first three terms of the expansion from (2)can be written as

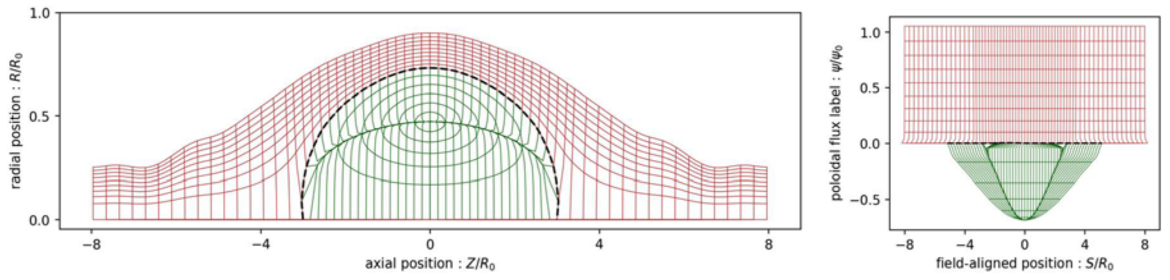

(a) (b)

FIG. 1. The simulation mesh in (a) real-space (b) field-aligned space. The SOL region is represented by red, and the core region is represented by green. The two regions are topologically separated by the separatrix, represented by the black dashed line. Only a subset of the usual grid is plotted for clarity in visualization. When the gyrokinetic model is used, a gap in the core region is made to avoid the magnetic null region due to gyrokinetic validity; however, this gap is not required when using the blended particle model and is not shown.

$$
\begin{aligned}
\alpha_0(v_\zeta^0) &= 1,\\
\alpha_1(v_\zeta^1) &= -\frac{mRv_\zeta}{q}\left(\frac{1}{n}\frac{\partial n}{\partial \psi} + \left(\frac{E}{T} - \frac{3}{2}\right)\frac{1}{T}\frac{\partial T}{\partial \psi}\right),\\
\alpha_2(v_\zeta^2) &= -\frac{m^2R^2v_\zeta^2}{q^2} \times \left[\left(\frac{E}{T} - \frac{3}{2}\right)\left(\frac{1}{n}\frac{\partial n}{\partial \psi}\frac{1}{T}\frac{\partial T}{\partial \psi}\right)\right.\\
&\quad + \frac{1}{2}\left(\frac{E^2}{T^2} - 5\frac{E}{T} + \frac{15}{4}\right)\left(\frac{1}{T}\frac{\partial T}{\partial \psi}\right)^2\\
&\quad \left. + \frac{1}{2}\left(\frac{1}{n}\frac{\partial^2 n}{\partial \psi^2} + \left(\frac{E}{T} - \frac{3}{2}\right)\frac{1}{T}\frac{\partial^2 T}{\partial \psi^2}\right)\right].
\end{aligned}
\tag{4}
$$

For the time-advance of the weight, i.e., Eq. (19), the quantity used is actually the partial derivative with respect to velocity. Assuming an expansion

$$
\begin{aligned}
\frac{\partial F_0(\tilde{\psi}, E)}{\partial \vec{v}} &\approx \frac{\partial}{\partial \vec{v}}\left[f_0(\psi, E)\left(\alpha_0(v_\zeta^0) + \alpha_1(v_\zeta^1) + \cdots\right)\right]\\
&\approx (1 + \alpha_1 + \alpha_2 + \cdots)\frac{\partial f_0}{\partial v}\\
&\quad + \left(\frac{\partial \alpha_1}{\partial v_\zeta} + \frac{\partial \alpha_2}{\partial v_\zeta} + \cdots\right) f_0.
\end{aligned}
\tag{5}
$$

To estimate the comparative largeness of the different terms of the expansion, the azimuthal velocity can be assumed comparable to the thermal velocity, and the average ratio for ions is $|q\psi|/m_i v_{th,i} R \approx 2$, while the average ratio for electrons is $|q\psi|/m_e v_{th,e} R \approx 300$. Currently, ANC uses only the lowest order expansion, which reduces to the expected form in the drift-kinetic limit as described in Sec. III. For ions, the large second order term is a departure from the usual gyrokinetics due to large finite Larmor radius, and further exploration of this effect is in progress.

B. Field aligned mesh

Although the physics of the code is formulated in cylindrical coordinates in order to couple regions across the magnetic separatrix, the simulation mesh itself is generated such that grid points lie along the magnetic field-lines. This allows for a coarser resolution in the direction parallel to the field-lines.

The field-aligned mesh is generated by picking points along the separatrix, then using the magnetic field directional unit vectors to assemble lines perpendicular to the magnetic field (along $\hat{\psi}$) and lines parallel to the magnetic field (along $\hat{S}$). Because of the differences between the two regions, the coordinate parallel to the field-line is defined differently for the core and SOL. These coordinates are only used in the interpolation of particles-to-mesh or mesh-to-particles.

For the core, $S = \pm 1$ is the location of the inner mid-plane where the mesh is periodically bound both physically and numerically while $S = 0$ is the location of the outer mid-plane. The field-aligned coordinate $S(\psi, \theta_{geo}) \equiv S(\psi(R, Z), \theta_{geo}(R, Z))$ is defined by the two independent variables, ψ (the poloidal flux label) and θ_{geo} (the geometric angle about the null-point).

For the SOL, $S = -1$ and $S = 1$ are the locations of the left and right boundaries, respectively, and $S = 0$ is the location of the outer mid-plane. The field-aligned coordinate $S(\psi, Z) \equiv S(\psi(R, Z), Z)$ is defined by the two independent variables, ψ (the poloidal flux label) and Z (the position along the axial direction).

In ANC, the mesh is field-aligned while the coordinate system is cylindrical with an unconventional signing, i.e.,

$$
\hat{R} \times \hat{Z} = \hat{\zeta}. \tag{6}
$$

Vector operations are obtained via chain rule and are numerically discretized via an assumed quadratic interpolant. In Secs. II B 1–II B 3, mesh operations are detailed, where X_ψ and X_S refer to physical spacing in the directions of $\hat{\psi}$ and $\hat{S} \equiv \hat{b}_0$.

Using the field-aligned mesh, a comparison of the growth-rate, frequency, and mode structure of a linear instability was performed and found to be consistent with results obtained via the cylindrically regular mesh.[7] Some benchmarks regarding the field-aligned mesh operations are also shown in the Appendix.

1. Partial derivatives

The mesh is generated by finding points along the magnetic field direction and along the direction, that is perpendicular to the magnetic field. The gradient, in this mesh, is then

$$
\vec{\nabla} f = \frac{\partial f}{\partial X_\psi}\hat{\psi} + \frac{\partial f}{\partial X_S}\hat{S} + \frac{1}{\partial R}\frac{\partial f}{\partial \zeta}\hat{\zeta}. \tag{7}
$$

Using this relation, the real space partial derivatives can be calculated by taking the scalar dot product

$$
\begin{aligned}
\frac{\partial f}{\partial R} &= \hat{R} \cdot \vec{\nabla} f = \frac{\partial f}{\partial X_\psi}\psi_R + \frac{\partial f}{\partial X_S}S_R,\\
\frac{\partial f}{\partial Z} &= \hat{Z} \cdot \vec{\nabla} f = \frac{\partial f}{\partial X_\psi}\psi_Z + \frac{\partial f}{\partial X_S}S_Z.
\end{aligned}
\tag{8}
$$

2. Gradient

Using the definitions of the partial derivatives, the real space gradient in cylindrical coordinates is

$$
\begin{aligned}
\vec{\nabla} f &= \frac{\partial f}{\partial R}\hat{R} + \frac{\partial f}{\partial Z}\hat{Z} + \frac{1}{\partial R}\frac{\partial f}{\partial \zeta}\hat{\zeta} = \left(\frac{\partial f}{\partial X_\psi}\psi_R + \frac{\partial f}{\partial X_S}S_R\right)\hat{R}\\
&\quad + \left(\frac{\partial f}{\partial X_\psi}\psi_Z + \frac{\partial f}{\partial X_S}S_Z\right)\hat{Z} + \frac{1}{\partial R}\frac{\partial f}{\partial \zeta}\hat{\zeta}.
\end{aligned}
\tag{9}
$$

3. Laplacian

Using the definition of the gradient, the Laplacian can be calculated from the following relation:

$$
\begin{aligned}
\nabla^2 f = \vec{\nabla} \cdot \vec{\nabla} f &= \frac{1}{R}\frac{\partial}{\partial R}\left(R(\hat{R} \cdot \vec{\nabla} f)\right)\\
&\quad + \frac{\partial}{\partial Z}\left(\hat{Z} \cdot \vec{\nabla} f\right) + \frac{1}{R}\frac{\partial}{\partial \zeta}\left(\hat{\zeta} \cdot \vec{\nabla} f\right).
\end{aligned}
\tag{10}
$$

Using the real space gradient operator given by (9) and some math, this relation becomes

$$
\begin{aligned}
\nabla^2 f &\to \frac{\partial^2 f}{\partial X_\psi^2} + \frac{\partial^2 f}{\partial X_S^2} + \frac{1}{R^2}\frac{\partial^2 f}{\partial \zeta^2} + (2\psi_R S_R + 2\psi_Z S_Z)\frac{\partial^2 f}{\partial X_\psi \partial X_S}\\
&\quad + \left(\frac{\partial \psi_R}{\partial R} + \frac{\partial \psi_Z}{\partial Z} + \frac{\psi_R}{R}\right)\frac{\partial f}{\partial X_\psi} + \left(\frac{\partial S_R}{\partial R} + \frac{\partial S_Z}{\partial Z} + \frac{S_R}{R}\right)\frac{\partial f}{\partial X_S}.
\end{aligned}
\tag{11}
$$

Finally, a perpendicular Laplacian operator can found by dropping the parallel derivatives, i.e., $\frac{\partial f}{\partial X_S} \rightarrow 0$, or by $\vec{\nabla}_\perp^2 \equiv \vec{\nabla} \cdot (\hat{b}_0 \times \vec{\nabla})$,

$$\nabla_\perp^2 f \rightarrow \frac{\partial^2 f}{\partial X_\psi^2} + \frac{1}{R^2}\frac{\partial^2 f}{\partial \zeta^2} + \left(\frac{\partial \psi_R}{\partial R} + \frac{\partial \psi_Z}{\partial Z} + \frac{\psi_R}{R}\right)\frac{\partial f}{\partial X_\psi}. \tag{12}$$

C. Toroidal wedge

Taking advantage of the symmetry of the FRC toroidal direction $\hat{\zeta}$ (azimuthal about the machine axis), ANC simulations use a truncated toroidal wedge based on the lowest common denominator, n_{LCD}, of the toroidal mode numbers kept in the simulation, i.e., going from a full torus $[0, 2\pi]$ to a truncated toroidal wedge $[0, 2\pi/n_{LCD}]$. This allows for physics of short toroidal wavelength modes to be fully resolved without waste in the case where simulations are focused on subsets of toroidal modes.

D. Magnetic field

To ensure that numerical heating or cooling of particles due to magnetic field quantities does not occur, a divergence-free magnetic field is ensured by representing all magnetic field related quantities through the derivatives of the poloidal flux. Through cubic spline representation of the poloidal flux, the magnetic field, defined as

$$\begin{aligned} \vec{B}_R &\equiv -\frac{1}{R}\frac{\partial \psi}{\partial Z}, \\ \vec{B}_Z &\equiv \frac{1}{R}\frac{\partial \psi}{\partial R}, \end{aligned} \tag{13}$$

will have a divergence that is analytically zero.

III. PARTICLE DYNAMICS

The particle-in-cell (PIC) method is conceptually simple: represent physical particles with simulation marker particles and follow their trajectories in the electrostatic (or electromagnetic) fields self-consistently calculated from these particle distributions. Mathematically, the marker particles follow the characteristics such that the phase-space volume represented by each particle does not change. Different models can be used to describe the particle dynamics suitable for different particle species. In ANC, particles can be described by a blended drift-Lorentz perturbative δf model or by a gyrokinetic perturbative δf model.

A. Blended drift-Lorentz particle model

Based on blended drift-Lorentz particle pusher introduced by Cohen *et al.*,[12] a drift-Lorentz perturbative δf particle model has been developed and implemented in ANC. Briefly described, the drift-Lorentz particle pusher is a Boris-push algorithm with corrections for time-steps large relative to the local cyclotron oscillation. These modified velocity and position updates are defined as

$$v^{n+1/2} = v^{n-1/2} + \Delta v_L^n + (1-\alpha)\Delta v_{\mu\nabla B}^n, \tag{14}$$

$$x^{n+1} = x^n + \Delta x_\parallel^{n+1/2} + \alpha\Delta x_\perp^{n+1/2} + (1-\alpha)\Delta x_d^{n+1/2}, \tag{15}$$

where $\Delta v_L \equiv q(\vec{E} + \vec{v} \times \vec{B_0})\Delta t$ is the change in velocity due to the normal Lorentz force, $\Delta v_{\mu\nabla B} \equiv -\mu\frac{\partial B}{\partial \vec{x}_\parallel}\Delta t$ is the change in velocity due to the magnetic mirror force, $\Delta x_\parallel \equiv \vec{v}_\parallel \Delta t$ and $\Delta x_\perp \equiv \vec{v}_\perp \Delta t$ are the changes in position due to parallel and perpendicular velocities, and $\Delta x_d \equiv (\vec{v}_E + \vec{v}_g + \vec{v}_c)\Delta t$ is the change in position due to drift velocity (composed of the drifts due to electric fields $\vec{v}_E \equiv \vec{E} \times \vec{B_0}/|B_0|^2$, magnetic field gradients $\vec{v}_g \equiv \frac{mv_\perp^2}{2qB_0}(\vec{B}_0 \times \vec{\nabla}B_0)/|B_0|^2$, and magnetic field curvature $\vec{v}_c \equiv \frac{mv_\parallel^2}{qB_0}(\vec{R}_c \times \vec{B}_0)/R_c^2|B_0|$). The blended parameter used in the position and velocity update equations is defined as

$$\alpha_s \equiv \frac{1}{\sqrt{1 + \left(\frac{\Omega_{c,s}\Delta t}{2}\right)^2}}. \tag{16}$$

Together, the particles described by this model follow a modified Vlasov equation:

$$\frac{d}{dt}f(\vec{x}, \vec{v}, t) \equiv \left[\frac{\partial}{\partial t} + \vec{v_{\mathit{eff}}} \cdot \vec{\nabla} + \vec{a_{\mathit{eff}}} \cdot \vec{\nabla}_v\right]f, \tag{17}$$

where the effective velocity and acceleration are shown in (14) and (15).

In the perturbed δf model,[13,14] the distribution function is split into $f \equiv f_0 + \delta f$, where f_0 is a known analytic equilibrium distribution such as the Maxwellian distribution and δf is the perturbation to this equilibrium distribution. When considering the moments of the distribution function as the main quantities of interest, the PIC method is essentially a series of Monte Carlo calculations, where the δf approach is a case of the control variates method.[15] Equation (17) can then be reformulated into the weight equation,

$$\begin{aligned} &\frac{d}{dt}\delta f = -\frac{d}{dt}f_0 \\ &\rightarrow \frac{d\tilde{w}}{dt} = -(1-\tilde{w})\frac{1}{f_0}\frac{df_0}{dt}, \end{aligned} \tag{18}$$

where $\tilde{w} \equiv \frac{\delta f/g}{f(0)/g(0)}$ and $g(t)$ is the marker distribution. Substituting from (17) and noting that portions due to the equilibrium distribution function are zero by definition, the weight equation becomes

$$\frac{d\tilde{w}}{dt} = -(1-\tilde{w})\frac{q}{m}\vec{E}_1 \cdot \frac{1}{f_0}\frac{\partial f_0}{\partial \vec{v}}. \tag{19}$$

Assuming an expansion of the equilibrium distribution function based on the local Maxwellian via Eq. (5),

$$\begin{aligned} \frac{\partial F_0(\tilde{\psi}, E)}{\partial \vec{v}} &\approx \left(\frac{\partial f_M}{\partial v} + \frac{\partial \alpha_1}{\partial v_\zeta}f_M\right) + \left(\alpha_1\frac{\partial f_M}{\partial v} + \frac{\partial \alpha_2}{\partial v_\zeta}f_M\right) + (\cdots) \\ &\approx f_M(\beta_0 + \beta_1 + \beta_2 + \cdots), \end{aligned} \tag{20}$$

where β_0 are terms of $\mathcal{O}\left(\left(\frac{mRv_\zeta}{q\psi}\right)^0\right)$, β_1 are terms of $\mathcal{O}\left(\left(\frac{mRv_\zeta}{q\psi}\right)^1\right)$, and so on, with ordering defined in Sec. II. More explicitly, the first order term is

$$\beta_0 \equiv -\frac{m_j}{T_j}(\vec{v_\parallel} + \alpha_j\vec{v_\perp}) - \frac{m_jR}{q_j}\left(\frac{1}{n_{j,0}}\frac{\partial n_{j,0}}{\partial \psi} + \left(\frac{E_j}{T_{j,0}} - \frac{3}{2}\right)\frac{1}{T_{j,0}}\frac{\partial T_{j,0}}{\partial \psi}\right)\hat{\zeta}, \tag{21}$$

where the subscript j refers to the particle species. In the explicit form of β_0, it can be seen that the contributions to the change in the perturbed distribution function is due to three effects: (1) the first term relates to the motion of the particles, most strongly the parallel direction; (2) the second term relates to the density gradient; (3) the third term relates to the temperature gradient. The current usage in ANC only includes the lowest order β_0 as a first step. Understanding the effect of the next order β_1, which is relatively large for ions, is in progress. It is also important to note the α_j factor in the velocity, which allows for the weight equation to reach its correct form in the two limits: (1) in the fully kinetic limit, the velocity is just the normal particle velocity; (2) in the drift-kinetic limit, the velocity reduces to just the parallel velocity.

B. Gyrokinetic particle model

Due its lineage from GTC, ANC has also implemented the standard gyrokinetic particle model. The dynamics of gyrokinetic particles are described by the Vlasov equation for guiding centers

$$\frac{d}{dt}f(\vec{X},\mu,v_{\parallel},t) \equiv \left[\frac{\partial}{\partial t} + \dot{\vec{X}}\cdot\vec{\nabla} + \dot{v_{\parallel}}\frac{\partial}{\partial v_{\parallel}}\right]f \tag{22}$$

with the velocity given by

$$\dot{\vec{X}} \equiv v_{\parallel}\hat{b}_0 + \vec{v_E} + v\vec{_{\nabla B}} + v\vec{_{R_c}}, \tag{23}$$

and the acceleration given by

$$\dot{v_{\parallel}} \equiv -\frac{1}{m}\left(\hat{b}_0 + \frac{v_{\parallel}}{\Omega_c}\nabla\times\hat{b}_0\right)\cdot(\mu\nabla B_0 + \nabla\phi). \tag{24}$$

Again, splitting the distribution function into perturbed and equilibrium components, the electrostatic gyrokinetic weight equation can be found:

$$\frac{d\tilde{w}}{dt} = -(1-\tilde{w}) - \left[\vec{v_E}\cdot\frac{\nabla f_0}{f_0} + \left(\left(\hat{b}_0 + \frac{v_{\parallel}}{\Omega_c}\nabla\times\hat{b}_0\right)\cdot\nabla\phi\right)\frac{1}{m}\frac{1}{f_0}\frac{\partial f_0}{\partial v_{\parallel}}\right]. \tag{25}$$

This is equivalent to the form given by Holod *et al.*[3] in the electrostatic approximation. The linear trajectories of gyrokinetic and drift-kinetic particles are equivalent. A difference between the gyrokinetic and drift-kinetic models comes from the particle-to-grid interpolation to calculate density. For gyrokinetic particles, the gyro-averaged density is calculated by using a four-point average approach, based on a ring with radius equal to gyroradius.[16,17] For drift-kinetic particles, the ring is reduced to the guiding center, and no gyro-averaging is performed. A second difference between the two models arises in the inclusion of a polarization density for gyrokinetic particles in the field solver as seen in (28).

IV. SELF-CONSISTENT FIELDS

Aside from the particle model, the other component of the PIC method is the self-consistent calculation of the electrostatic (or electromagnetic fields) fields arising from the particle distributions. Currently in ANC, only the electrostatic approximation is considered.

A. Blended Poisson equation

To obtain the electric fields used to advance particle velocities, the electrostatic potential is found through solving the Poisson equation in ANC.

The form of the Poisson equation, complementary to the blended mover,[12] is

$$\begin{aligned}-\left[\lambda_{de}^2\nabla^2\phi + (1-\alpha_e)\rho_e^2\nabla_{\perp}^2 + (1-\alpha_i)\rho_i^2\nabla_{\perp}^2\right]\frac{e\phi}{T_e} \\ = \left(\frac{n_{i,0}+\delta n_i}{n_0}\right) - \left(\frac{n_{e,0}+\delta n_e}{n_0}\right),\end{aligned} \tag{26}$$

where the first term on the LHS is Debye shielding, the second and third terms on the LHS are electron and ion polarization densities, respectively, and the two terms on the RHS are the electron and ion densities. Note that the blended parameter modifies the polarization densities because the polarization densities are self-consistently contained within the RHS densities when the blended model approaches the fully kinetic representation.

B. Quasi-neutral blended Poisson equation

For the turbulence studies that is the focus of ANC, space-charge waves, such as the electron plasma wave, constrain the simulation time step but are not physically interesting. In gyrokinetics, the quasi-neutrality equation, sometimes called the gyrokinetic Poisson equation, is solved instead of the full Poisson equation

$$-\left[(1-\alpha_e)\rho_e^2\nabla_{\perp}^2 + (1-\alpha_i)\rho_i^2\nabla_{\perp}^2\right]\frac{e\phi}{T_e} = \left(\frac{\delta n_i}{n_0}\right) - \left(\frac{\delta n_e}{n_0}\right), \tag{27}$$

where the Debye shielding term is dropped and the equilibrium ion and electron densities are assumed to be equal due to quasi-neutrality. This removes the space-charge waves from the simulation model and is sufficient only if there is a particle species away from the fully kinetic limit to provide a finite polarization term. This equation is insufficient when this is not the case and is discussed in Sec. IV C.

In the case, where the gyrokinetic model, described in Sec. III, is used for the ions, the quasi-neutrality equation[3] solved depends on the ion polarization term only. That is,

$$-\rho_i^2\nabla_{\perp}^2\frac{e\phi}{T_e} = \left\langle\frac{\delta n_i}{n_0}\right\rangle - \left\langle\frac{\delta n_e}{n_0}\right\rangle, \tag{28}$$

where the $\langle\cdots\rangle$ represents the gyro-averaged (via gyro-sampling) quantities. This equation can be seen as (27) in the limit of relevant time-scales being slower than cyclotron oscillations ($\Omega_{ce}\Delta t, \Omega_{ci}\Delta \gg 1 \rightarrow \alpha_e, \alpha_i \approx 1$) and relevant length scales being larger than electron gyroradii ($k_{\perp}^2\rho_e^2 \ll k_{\perp}^2\rho_i^2$).

C. Quasi-neutral blended Poisson equation with partial adiabatic response

In the FRC, there are regions of extremely low magnetic field strength. As such, there are locations where the blended particle model will effectively be a fully kinetic representation for all simulated particle species. In such case, the polarization terms on the LHS of (27) will decrease to zero due to the blended parameter. On the other hand, there is no guarantee for the densities on the RHS to cancel to zero as well. Without the Debye shielding term, trying to solve (27) for the electrostatic potential ϕ in this limit is a source of numerical issues. To avoid this problem while maintaining quasi-neutrality, a portion of the electron response is assumed adiabatic:

$$\frac{\delta f_e}{f_e}(v > v_{cut-off}) = \frac{e\phi}{T_e} f_0. \tag{29}$$

The assumption of a cutoff velocity is essentially an assumption of a cutoff frequency based on

$$\omega < k_\parallel v_{cut-off}, \tag{30}$$

where the condition is based on $k_\parallel$ of the mode structure and the selected cutoff velocity. For the turbulence studies of interest, this cutoff frequency is unlikely to affect the possible wave-particle resonances, and variation of the assumed cutoff velocity will be used to confirm convergence on resultant physics. With this partial adiabatic assumption and assuming the equilibrium particle densities to be equal, the form of the quasi-neutrality equation changes to

$$-\left[(1-\alpha_e)\rho_e^2\nabla_\perp^2 + (1-\alpha_i)\rho_i^2\nabla_\perp^2 - \gamma_A\right]\frac{e\phi(k_\parallel \neq 0)}{T_e} = \left(\frac{\delta n_i}{n_0}\right) - \left(\frac{\delta n_e}{n_0}\right), \tag{31}$$

where γ_A and γ_{NA} are the fractions of the electrons assumed to be adiabatic and non-adiabatic, calculated by

$$\begin{aligned}\gamma_{NA} &= \mathrm{erf}(v_{cut-off}/v_{th}),\\ \gamma_A &= 1-\gamma_{NA},\end{aligned} \tag{32}$$

where v_{th} is the local thermal velocity. Note that this equation is only valid for the component of electrostatic potential with finite $k_\parallel$ due to the adiabatic response. A second quasi-neutrality equation without the adiabatic response must now be solved for the component of electrostatic potential with $k_\parallel = 0$,

$$-\left\langle\left[(1-\alpha_e)\rho_e^2\nabla_\perp^2 + (1-\alpha_i)\rho_i^2\nabla_\perp^2\right]\right\rangle\frac{e\phi(k_\parallel = 0)}{T_e} = \left\langle\left(\frac{\delta n_i}{n_0}\right) - \left(\frac{\delta n_e}{n_0}\right)\right\rangle, \tag{33}$$

where $\langle\cdots\rangle$ denotes a field-line average. Because the magnetic field is not uniformly small along the field-lines in the problematic null magnetic field regions of the FRC, this field-line average is sufficient to ensure that the LHS remain finite. The scenario that the LHS falls to zero due to small simulation time-steps requires the Debye shielding term but is outside of the interest of this model. The total electrostatic potential is then found by combining the results of the two equations:

$$\phi(k_\parallel) = \phi(k_\parallel = 0) + \phi(k_\parallel \neq 0). \tag{34}$$

V. BENCHMARKS

Several benchmarks against analytic theory have been performed with ANC. These benchmarks use a simple uniform magnetic equilibrium for analytic simplicity. The routines and functions called within ANC are almost exactly the same set as in more complicated FRC equilibria; thus, these benchmarks provide some measure of confidence in the implementation of the physics outlined in Secs. I–IV.

A. Drift-wave

Using a simple straight magnetic field with varying density, the drift-wave dispersion is found from simulation and compared to analytic theory.

With (1) the gyro-kinetic ion model and drift-kinetic electron model; (2) flat temperatures but non-uniform density; and (3) a simple straight uniform magnetic field, the dispersion of the drift wave is

$$\begin{aligned}0 = 1 - \Bigg[\left(\frac{1+b}{b}\right)\Bigg(&-k_\perp\rho_i\frac{\kappa_n}{\sqrt{2}k_\parallel}\Lambda_0(b)Z\left(\frac{\omega/\Omega_{c,i}}{\sqrt{2}k_\parallel\rho_i}\right)\\ &+\frac{1}{2}\Lambda_0(b)Z'\left(\frac{\omega/\Omega_{c,i}}{\sqrt{2}k_\parallel\rho_i}\right) + k_\perp\rho_e\frac{\kappa_n}{\sqrt{2}k_\parallel}\frac{T_i}{T_e}Z\left(\frac{\omega/\Omega_{c,i}}{\sqrt{2}k_\parallel\rho_e}\right)\\ &-\frac{1}{2}\frac{T_i}{T_e}Z'\left(\frac{\omega/\Omega_{c,i}}{\sqrt{2}k_\parallel\rho_e}\right)\Bigg)\Bigg],\end{aligned} \tag{35}$$

where $Z\left(\frac{\omega/\Omega_{c,i}}{\sqrt{2}k_\parallel\rho_i}\right)$ is the plasma dispersion function, $\Lambda_0(b) \equiv I_0(b)\exp(-b)$ is the exponentially scaled modified Bessel function of the first kind, $b \equiv k_\perp^2\rho_i^2$, and $\kappa_n \equiv -\nabla n/n$ is the density gradient inverse scale length.

In Fig. 2, the numerical solutions of the analytic theory (35) is plotted as the dashed line, while the normalized 2D spectral power shows the ANC simulation results. Three models in ANC are tested and shown: (a) gyrokinetic ions with drift-kinetic electrons, (b) gyrokinetic ions with adiabatic electron response, and (c) blended drift-Lorentz ions with adiabatic electron response. The simulation results agree with the theoretical dispersion relation at long wavelengths due to better numerical resolution and because shorter wavelengths (for the blended drift-Lorentz case (c), $|k_\parallel\rho_i| > 4.2\times10^{-5}$) are numerically smoothed. This verifies the capability to simulate drift-waves in ANC.

B. Ion acoustic wave

Using a simple straight magnetic field without pressure gradients, the ion-acoustic wave dispersion is found from simulation and compared to analytic theory.

With (1) the fully kinetic ion model with an adiabatic electron response; (2) flat temperatures and density; (3) a simple straight uniform magnetic field; and (4) the assumption of $k_\perp = 0$, the dispersion of the ion acoustic wave is

$$0 = 1 - \frac{1}{2}\frac{T_e}{T_i}Z'\left(\frac{\omega/\Omega_{c,i}}{\sqrt{2}k_\parallel\rho_i}\right), \tag{36}$$

where $Z\left(\frac{\omega/\Omega_{c,i}}{\sqrt{2}k_\parallel\rho_i}\right)$ is the plasma dispersion function.

In Fig. 3, the numerical solution of the analytic theory (36) is plotted as dashed lines, while the normalized 2D spectral power shows the ANC simulation results. The simulation results using the blended ion and adiabatic electron response agree with the theoretical dispersion relation. This verifies the capability to properly simulate waves in the parallel direction in ANC.

C. Ion Bernstein wave

Using a simple straight magnetic field without pressure gradients, the ion Bernstein wave dispersion is found from simulation and compared to analytic theory.

With (1) the fully kinetic ion model with an adiabatic electron response; (2) flat temperatures and density; (3) a simple straight

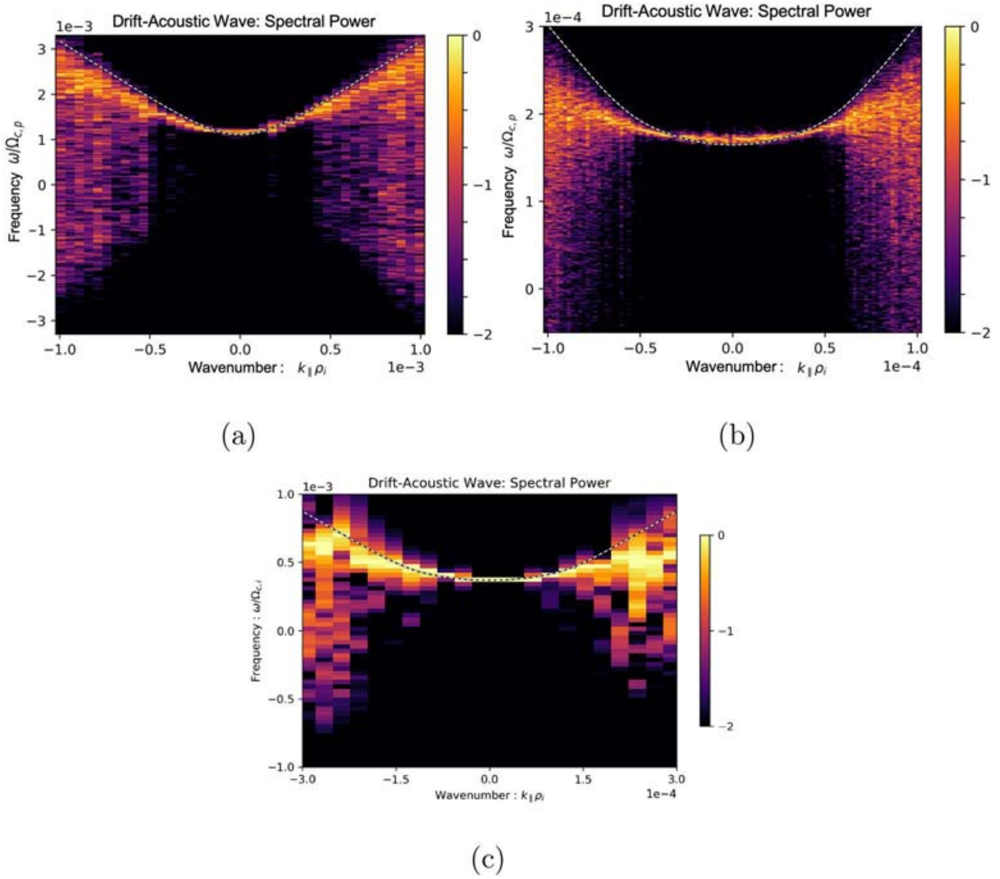

(a) (b)

(c)

FIG. 2. Analytic theory (dashed line) of the drift-wave is plotted on top of spectral power found from ANC simulation using three different models: (a) gyrokinetic ions with drift-kinetic electrons, (b) gyrokinetic ions with an adiabatic electron response, and (c) blended ions with an adiabatic electron response. The simulation results are consistent with theory, tracking along the drift-wave frequency which is shifted away from zero. At shorter wavelengths (for example, in the blended case (c), $|k_\parallel \rho_i| > 4.2 \times 10^{-5}$), simulation deviates from theory due to the lower numerical resolution as well as numerical smoothing which was used in this simulation.

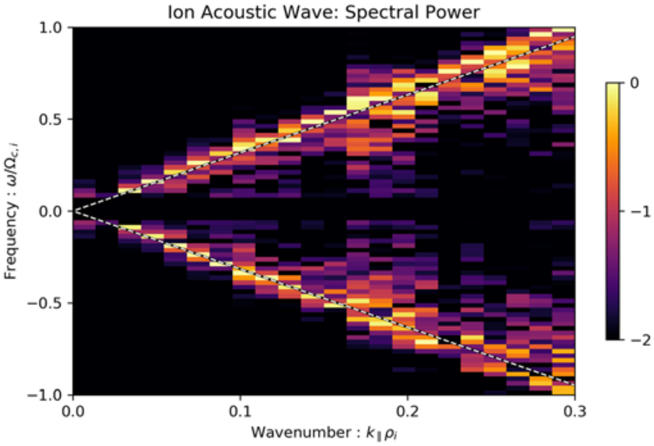

FIG. 3. Analytic theory (dashed line) of the ion acoustic wave is plotted on top of spectral power found from ANC simulation. The simulation results are consistent with theory, tracking along the correct slope of the ion acoustic wave.

uniform magnetic field; and (4) the assumption of $k_\parallel \sim 0 \ll k_\perp$, the dispersion of the so-called neutralized Ion Bernstein mode[18] is

$$0 = 1 - 2\frac{T_e}{T_i}\sum_{n=1}^{\infty}\Lambda_n(b)\frac{n^2\Omega_{c,i}^2}{\omega^2 - n^2\Omega_{c,i}^2}, \qquad (37)$$

where $\Lambda_n(b) \equiv I_n(b)\exp(-b)$ is the exponentially scaled modified Bessel function of the first kind and $b \equiv k_\perp^2 \rho_i^2$. In the simulation, the electron response is explicitly set to be adiabatic while the ions use the blended particle model. Although only the component with $k_\parallel = 0$ is kept, the adiabatic electron response assumption is consistent between the shown dispersion relation and within this simulation. This benchmark is designed to show the fully kinetic physics capability of the blended model in the perpendicular direction whereas the previous gyrokinetic model would not include such physics.

In Fig. 4, the numerical solution of the analytic theory (37) is plotted as dashed lines, while the normalized 2D spectral power shows the ANC simulation. While the higher frequency branches are captured by the simulation, the resolution used only roughly resolves the

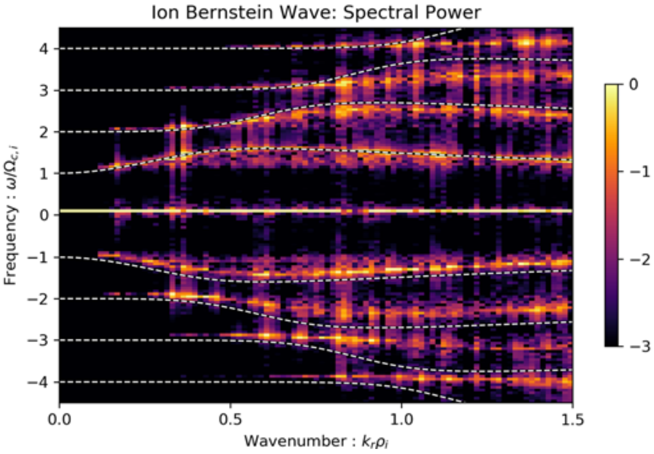

FIG. 4. Analytic theory (dashed line) of the so-called neutralized Ion Bernstein mode is plotted on top of spectral power found from ANC simulation. The simulation results are consistent with theory, tracking along the frequencies which are shifted away from the cyclotron harmonic resonances.

first branch at longer wavelengths. This verifies the capability to properly simulate waves available only in the fully kinetic model in ANC.

Note that the same benchmark was also performed with the fully-kinetic ion model. In that benchmark, a much smaller time step must be used; otherwise, numerical instability arises from the under-resolved higher frequency branches. On the other hand, in the blended ion model benchmark, larger time steps can be taken because the blended ion model becomes more drift-kinetic-like and the physics of the Bernstein mode will be unavailable to under-resolve. This highlights a benefit of the blended model in which the relevant physics can be chosen by choosing the simulation time step.

D. Lower-hybrid wave

Using a simple straight magnetic field with non-uniform density, the lower-hybrid wave is probed by external antenna excitation to compare the plasma response from simulation with analytic theory.

With the fully kinetic ion model with non-adiabatic kinetic electron model and assumption of $k_\parallel \ll k_\perp$, the dispersion of the lower-hybrid wave is

$$\omega^2 = \omega_{LH}^2\left(1 + \frac{m_i}{m_e}\frac{k_\parallel^2}{k_\perp^2}\right), \tag{38}$$

where the lower-hybrid frequency is defined by

$$\omega_{LH}^2 \equiv \left(\frac{1}{\omega_{pi}^2 + \omega_{pe}^2} + \frac{1}{\Omega_{c,i}\Omega_{c,e}}\right)^{-2}. \tag{39}$$

An external electrostatic potential ($\phi_{ext} \propto \cos(\omega_0 t)$) is imposed on the plasma and causes the self-consistent electrostatic potential to grow linearly when the antenna frequency is near an eigenfrequency, much like forced harmonic oscillation. In this case, a range of eigenfrequencies exists and the response is not as sharp as might be expected, though the largest response lies in the range defined by the standard deviations of the mean frequency from (38). Due to the non-uniform density and non-local domain ($k_\zeta = n/R$), there is a range of possible solutions to the dispersion (38), depicted as the shaded region in Fig. 5. In the same figure, plasma response from external antenna excitation at five different frequencies is shown. This verifies the capability to properly simulate waves available only in the fully kinetic model in ANC with both blended ions and electrons.

VI. INITIAL BLENDED FRC SIMULATION RESULTS

Recently, simulations using blended thermal ions and electrons have been performed, and the preliminary results are reported here. Eight toroidal modes are kept ($n = [0, 10, \ldots, 60, 70]$) in the simulations shown. Similar results were obtained (but not shown here) for simulations with only four toroidal modes kept ($n = [0, 25, 50, 75]$). As a first step, no equilibrium electric field profile is used in these simulations despite the existence of equilibrium electric fields in experiment.

The density profile used in these simulations is shown in Fig. 6. The temperature profiles follow the shape of the density profiles, i.e., $\eta_i = \eta_e = 1$ where $\eta_i \equiv L_{T,i}^{-1}/L_n^{-1}$ and $\eta_e \equiv L_{T,e}^{-1}/L_n^{-1}$, and the maximum ion and electron temperatures are $T_{i,max} = 400$ and $T_{e,max} = 80$ eV. Although the density and temperature profiles are assumed to be flux-functions in these simulations, true FRC equilibrium profiles are surface-functions which may differ from flux-functions after accounting for toroidal rotation.

From the simulation parameters, ions are effectively represented as fully kinetic particles with $\alpha_i = 1$ throughout the simulation domain such that the correction terms are negligible. For non-adiabatic electrons, however, α_e is much more interesting and shown in Fig. 7: in the core along the region of lowest magnetic field, $\alpha_e \sim 1$ such that electrons are represented as fully kinetic particles; in the SOL, $\alpha \approx 0$–0.5 such that electrons are represented as drift-kinetic particles.

A. Initial results

Consistent with previous work, instability only forms in the SOL. This instability has higher toroidal mode numbers ($n = [60, 70]$,

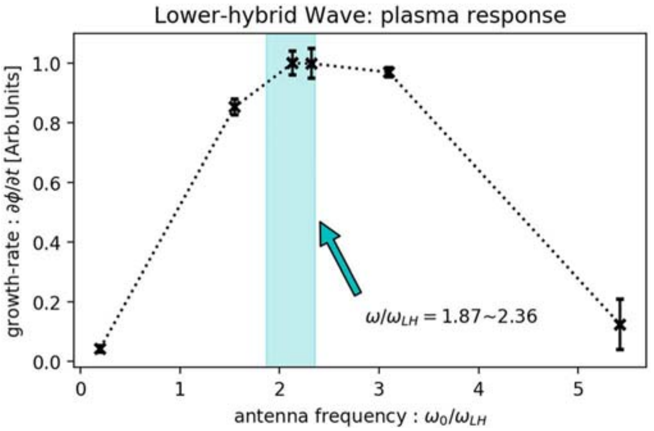

FIG. 5. Analytic theory (range depicted by cyan shaded region) of the lower-hybrid wave is plotted on top of plasma response found from ANC simulation (represented by fits to the initial linear rate of increase in potential due to resonance with the antenna). The simulation results are consistent with theory with strongest response in the range of frequencies expected by analytic theory.

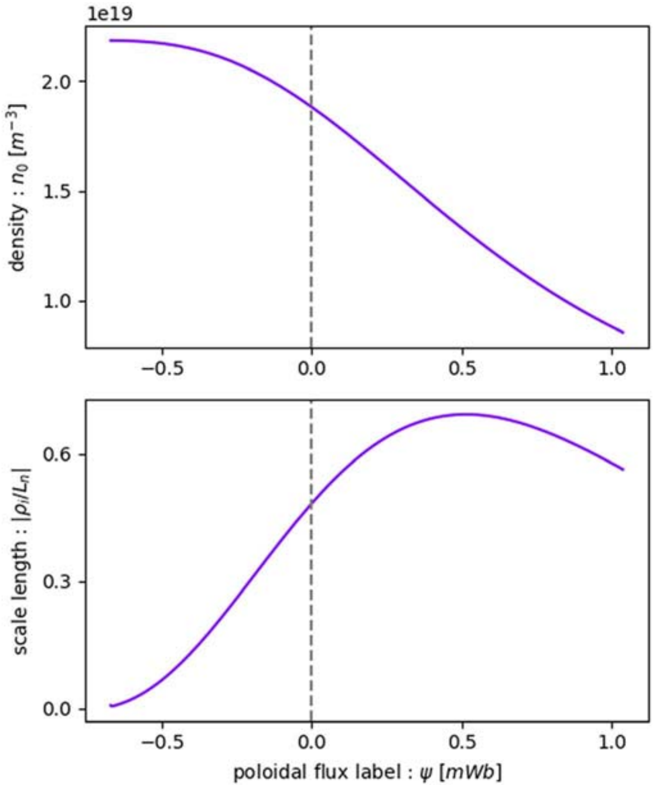

FIG. 6. The density profile used in the simulation is shown in the top while the inverse scale length normalized by ion gyro-radius ($\rho_i \equiv \frac{\sqrt{m_i T_i}}{eB_0}$) is shown in the bottom. The dashed gray line represents the separatrix.

corresponding to $\langle k_\zeta \rho_i \rangle > 10$), and is shown in Fig. 8. During the initial linear growth stage, the instability for mode numbers $n = [60, 70]$ has real frequency $\omega_r/\Omega_{c,p} = [0.52, 0.56]$ and linear growth-rate $\gamma/\Omega_{c,p} = [0.11, 0.11]$. The mode rotates in the direction of the ion diamagnetic drift, and the frequency is comparable to the so-called unconventional short wavelength ion temperature gradient (SWITG) mode.[19–21] Initial analysis of the non-adiabatic electron response peaks when the mode frequency is roughly equal to the electron magnetic gradient drift frequency, suggesting that this mode is, at least, partially driven by the electron grad-B motion.

As the instability saturates, there is an inverse spectral cascade from the higher to lower toroidal wavenumbers. This can be seen as the change from the shorter wavelength mode structure in Fig. 8 to the larger eddies in Fig. 9. Compared with the previous gyrokinetic turbulence simulations,[8] there is less inward spread from SOL to core; however, it is difficult to discern whether this is due to the correct representation of particle trajectories or the change in the nature of the instability due to the inclusion of the non-adiabatic electron response. After saturation, the amplitude of fluctuations in the core are about two orders of magnitude below the SOL at longer wavelengths, similar to the gyrokinetic turbulence simulations.

Simulations using more realistic profiles (including equilibrium electric fields) reconstructed from experimental shots are ongoing and will be reported on, in detail in future work.

VII. DISCUSSION

To address the coupled nature of the core and edge regions of field-reversed configuration plasmas, a formulation for electrostatic particle simulation across the separatrix is presented. A field-aligned simulation mesh and corresponding mesh operations have been developed and verified. A formulation for efficient particle pushing, free from gyrokinetic validity and based on the blended particle model, is also established. A corresponding quasi-neutrality equation for self-consistent fields is also detailed. Using about 2.5×10^6 cells and 19×10^6 particles, a total wall-time of roughly 2500 node-hours was required for this numerically converged blended FRC simulation run, comparable to previous gyrokinetic FRC simulation runs. For magnetic geometry with large variations in magnetic field magnitude, this model is an improvement in simulation time over the fully kinetic particle model and an improvement in model validity over the gyrokinetic model. The efficient use of the blended model for turbulent transport simulations will aided by the upcoming exascale computing platforms. All of these new features have been implemented in ANC and benchmarked in simple cylindrical geometry. Nonlinear simulations in FRC geometry have also been performed.

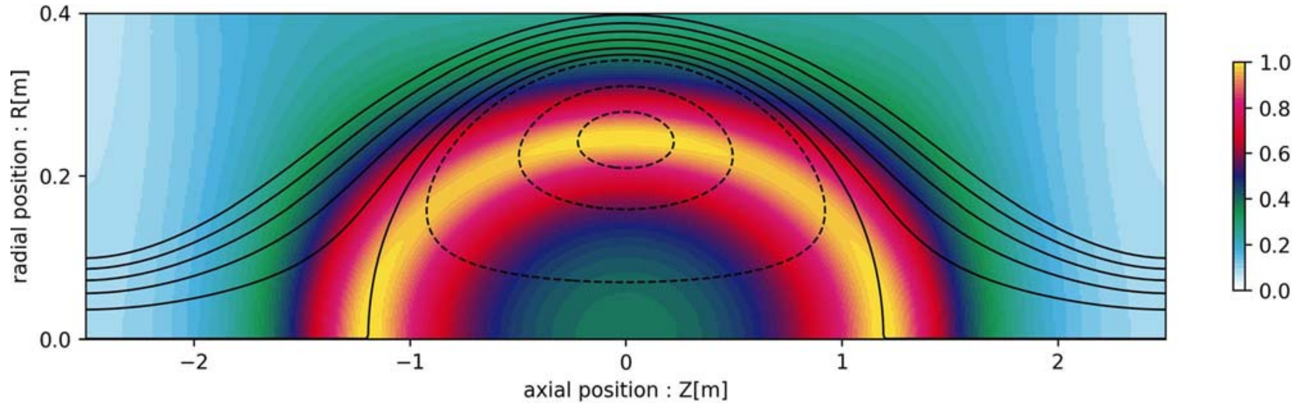

FIG. 7. The electron α_e, calculated by (16) for the simulation parameters, is shown. Electrons are fully-kinetic-like ($\alpha_e \sim 1$) where the magnetic field is low but are drift-kinetic-like ($\alpha_e < 1$) where the magnetic field is larger.

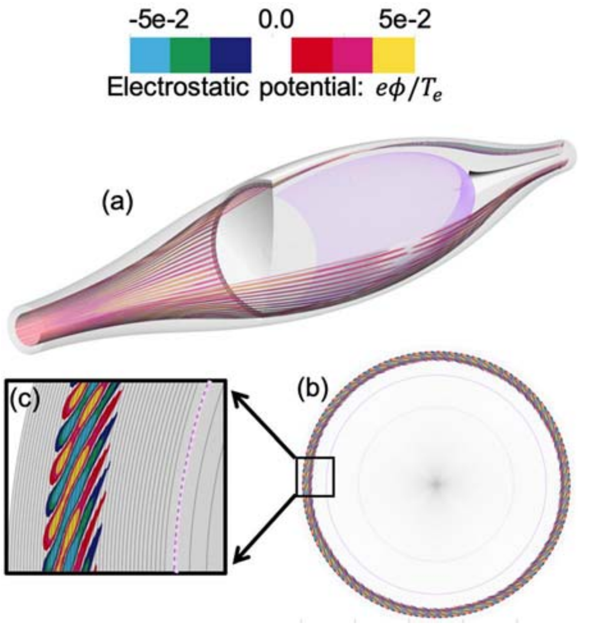

FIG. 8. The 3D electrostatic potential during linear growth is shown. The top (a) shows full (R, Z, ζ) view where the gray region shows the extent of the simulation domain, and the purple shell represents the separatrix surface marking the separation of the core and SOL regions. The cut on the left side of (a) is shown in the 2D slice on the bottom right (b). A zoomed in view on the bottom left (c) shows the short wavelength mode structure where the dashed line represents the separatrix.

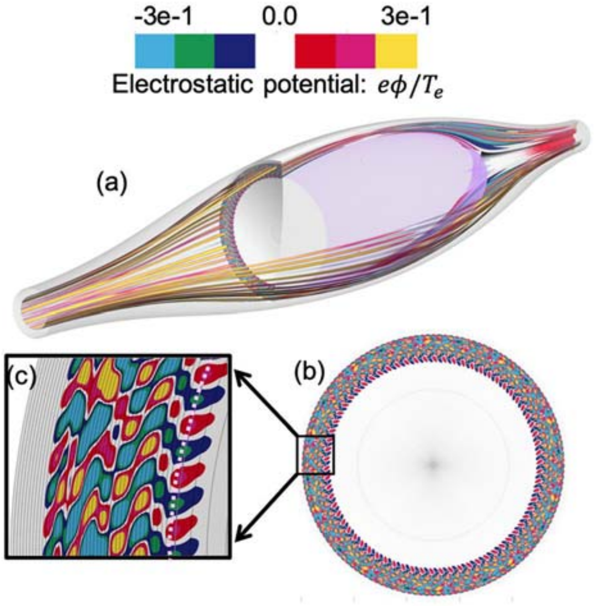

FIG. 9. The 3D electrostatic potential after nonlinear saturation is shown. The top (a) shows full (R, Z, ζ) view where the gray region shows the extent of the simulation domain, and the purple shell represents the separatrix surface marking the separation of the core and SOL regions. The cut on the left side of (a) is shown in the 2D slice on the bottom right (b). A zoomed in view on the bottom left (c) shows the turbulent eddies where the dashed line in purple represents the separatrix.

Previous results from GTC and ANC represent, to date, the only first principles gyrokinetic turbulence simulations[7–9] in realistic FRC geometry. The non-local simulation domain spanning across the separatrix represented an extension from the earlier local linear gyrokinetic simulations. The initial FRC blended model simulation results presented in this paper are another step in the progress toward more realistic FRC turbulence simulations. The effects of fully kinetic ion orbits and non-adiabatic electron response are observed. Magnetic perturbations, which can affect the field-line structure of the FRC, are not yet included in this model.

In agreement with past work, no linear ion-scale instabilities develop in the FRC core, likely suppressed by the large ion orbits (finite Larmor radius effect). Overall fluctuation levels are also much lower than in the SOL, though details of inward spread are still under consideration. In the SOL, a linear instability develops at short wavelengths, eventually leading to an inverse spectral cascade to longer wavelengths as well as an inward spread from SOL to core. These preliminary results are consistent with previous findings.

The goal of these first principles FRC simulations is understand transport scaling for the realization of a fusion reactor based on the FRC concept. This is the motivation for the inclusion of the non-adiabatic electron response, which enables the calculation of particle diffusivity and electron thermal conductivity. Electron heat flux due to the self-consistent fluctuations can be calculated within the simulation via $\vec{q}_e \cdot \hat{\psi} \equiv \int \delta f_e (\frac{1}{2} m_e |\vec{v}|^2 - \frac{3}{2} T_{e,0})(\vec{v}_E \cdot \hat{\psi}) dv$, noting that this only takes into account the effect of the collisionless fluctuations. This heat flux can then be used to calculate the conductivity from Fick's law $\chi_e = \vec{q}_e \cdot \hat{\psi} / (n_{e,0} \vec{\nabla} T_{e,0} \cdot \hat{\psi})$. Finally, from the conductivity, the perpendicular core energy confinement time can be estimated by $\tau_{E,e} = R_S^2 / \langle \chi_e \rangle$, where R_S is the separatrix radius and $\langle \chi_e \rangle$ is the conductivity averaged over the post-saturation duration, in the toroidal direction, and in the field-line direction. Despite lacking several effects known to exist in the experiment, perpendicular energy confinement time in the core is estimated to be ∼1 ms in the preliminary FRC simulations shown in this paper, a surprisingly reasonable estimate when compared with the experiments.[22,23] It should be noted that the simulations shown have not incorporated beam ions and equilibrium electric fields, both of which can significantly modify the properties of possible instabilities and the saturated level. These estimates will be reevaluated as further effects are included.

Validating the fluctuation spectra and transport calculations against the current experiments is a necessary step before transport scaling can be understood. Immediate efforts in the future are toward ongoing FRC blended model simulations based on reconstructed experimental equilibria. These ongoing simulations also feature the effect of equilibrium electric field, an important experimentally available tool. Other future physics development priorities include parallel sheath boundary conditions and electromagnetic effects. In addition, with the upcoming exascale computing platforms in mind, upgrades for GPU acceleration using OpenACC directives are ongoing.

ACKNOWLEDGMENTS

The authors would like to thank the TAE team at TAE Technologies, Inc., for equilibrium data as well as ongoing insights and for the continued development of this simulation model. Initial development began at University of California, Irvine with the support of the Norman Rostoker Fellowship (Grant No. TAE-200441). Further development and simulations used the resources of DOE Office of Science User Facilities: National Energy Research Scientific Computing Center (DOE Contract No. DE-AC02–05CH11231) and Innovative and Novel Computational Impact on Theory and Experiment (INCITE) program at Argonne Leadership Computing Facility at Argonne National Laboratory (DOE Contract No. DE-AC02–06CH11357).

APPENDIX: FIELD-ALIGNED MESH OPERATION BENCHMARKS

A. Grid operations

Using test functions, comparisons are made for the mesh operations in the field-aligned and regular meshes. The results for the field-aligned mesh operations are from ANC directly while the results from the regular mesh operations are from Python using the NumPy library.

In Figs. 10(a) and 10(b), the partial derivatives with respect to the radial and axial directions, respectively, are shown. These partial derivatives are used for the calculation of the electric field from the self-consistently solved electrostatic potential, which is then used to push simulation particles. The field-aligned mesh operations agree with the regular mesh operations both qualitatively and quantitatively.

In ANC, either the full Laplacian or the perpendicular Laplacian can be used to solve for the self-consistent electrostatic potential from the quasi-neutrality equation. In Fig. 10(c), the full Laplacian is shown. The field-aligned mesh operation agrees with the regular mesh operations both qualitatively and quantitatively.

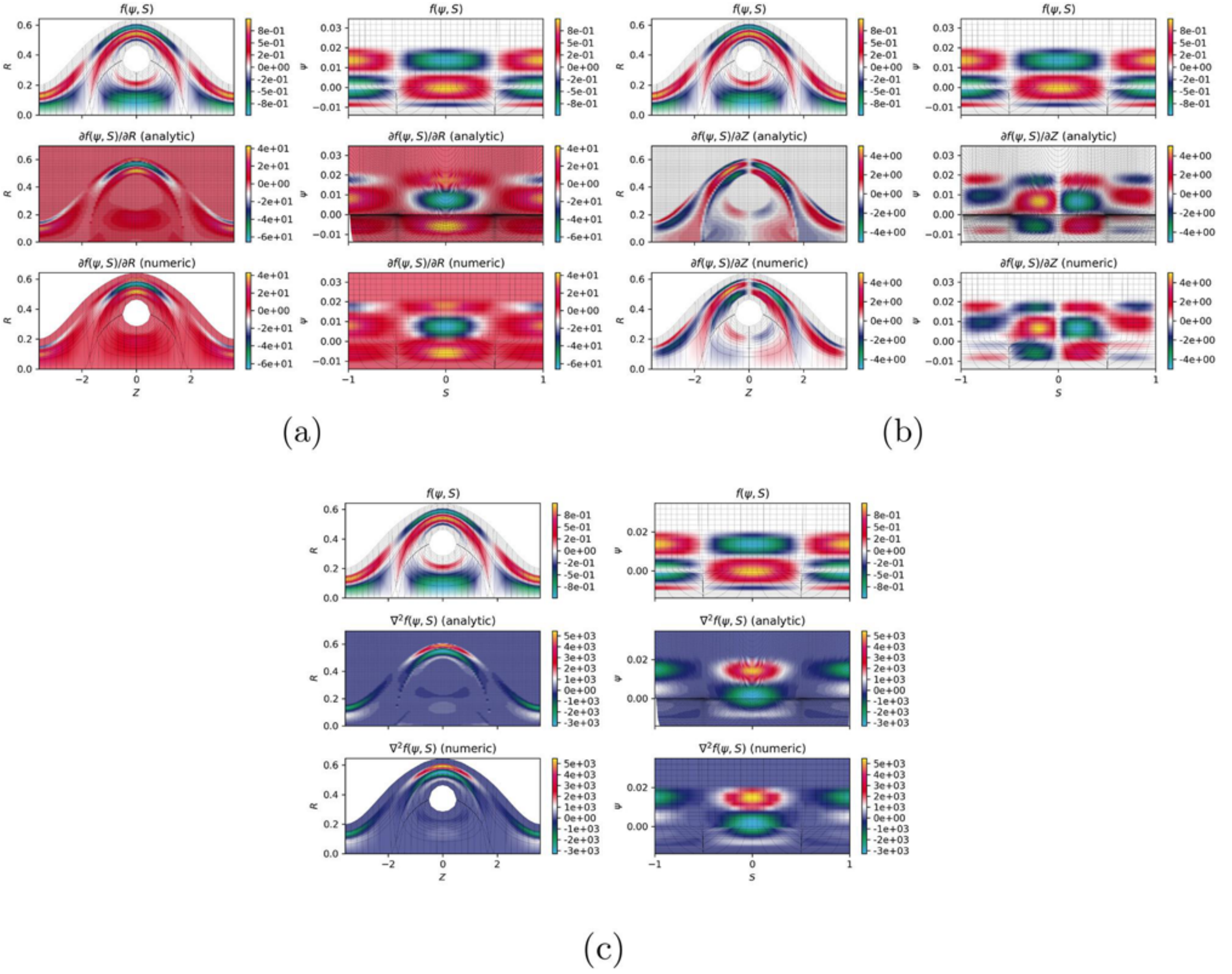

(a)

(b)

(c)

FIG. 10. Comparisons of three different mesh operations are shown: (a) the partial derivative with respect to the radial coordinate R, (b) the partial derivative with respect to the axial coordinate Z, and (c) the Laplacian. A test function of form $f(\psi, S) \propto \cos(k_\psi \psi)\cos(k_S S)$ is shown in the real space mesh (top left) and in the field-aligned mesh (top right). A mesh operation is calculated in the cylindrical mesh and is shown in the real space mesh (mid-left) and in the field-aligned mesh (mid-right). The same mesh operation is calculated in the field-aligned mesh and is shown in the real space mesh (bottom left) and in the field-aligned mesh (bottom right).

In general, the ANC field-aligned mesh operations also impose zero on the machine axis. This causes a slight discrepancy in the comparison of the partial derivative with respect to the axial position.

B. Mesh to particle interpolation

Using a test function for the electric field, comparisons are made for electron dynamics. The "grid interp." results are updated using electric field components interpolated onto particles using field-aligned mesh operations while "direct calc." results are updated using electric field components directly calculated from the analytic test function. Three different grid resolutions are used in the case of "grid interp.," with the cell shapes being shown in corresponding colors in (a) of Fig. 11. Electrons are tracked near the turning points of the core where the most concern may be for stretched meshes; these electrons cross multiple simulation cells in this benchmark.

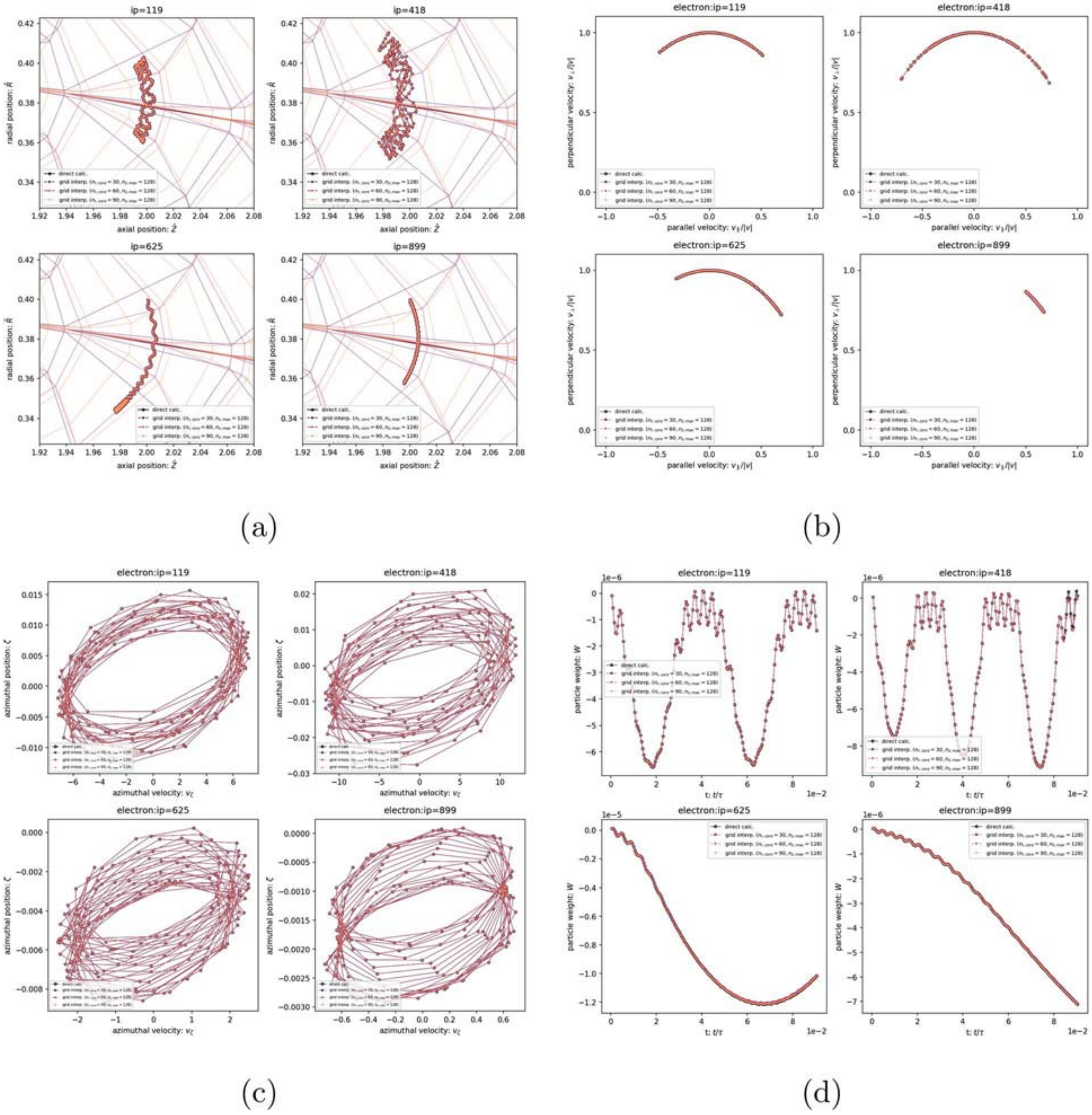

(a)

(b)

(c)

(d)

FIG. 11. Comparisons of electron dynamics are shown: (a) R-Z trajectory in the poloidal plane with corresponding simulation meshes shown in matching colors, (b) parallel vs perpendicular velocity, (c) toroidal phase space, and (d) weight evolution over time. Four different tracked electrons (ip is the tracking label of the particle) are shown for the one direct calculation case and the three mesh-to-particle interpolation cases.

In Fig. 11, the results of these comparison tests are shown: (a) poloidal plane R-Z trajectories of electrons near or at the turning point of the FRC core; (b) velocity space, parallel and perpendicular relative to the magnetic field, which shows that the electrons have not changed in energy much during this time (magnitude stays almost constant here); (c) toroidal phase space, which shows a slight toroidal drift; and (d) the delta-f weight evolution over time. The grid cells are also plotted in the corresponding color for context (not shown for the direct calculation case since it does not matter), and "ip" is the tracking label of the particle. Only a subset of the electrons tracked are shown to avoid confusion.

With respect to interpolation from field-aligned mesh to particles, note that position updates are indirectly affected via velocity, the velocity updates are directly affected, and the delta-f weight updates are both directly affected and indirectly affected via position and velocity. The R-Z trajectory, the azimuthal phase space, and the velocity space are all indistinguishable (10^{-6}%–10^{-5} % difference for positions and 10^{-4}%–10^{-3} % difference for velocities, when compared to the direct calculation). On the other hand, the delta-f weight has some noticeable differences ($0.1\% - 1\%$ difference, when compared to the direct calculation) since it is more sensitive to the velocity and position differences. In all aspects, these differences decrease as the grid resolution is increased as expected. For this particular case of this test function, no significant change is seen when increasing the number of ψ cells in the core from 60 to 90.

DATA AVAILABILITY

The data that support the findings of this study are available from the corresponding author upon reasonable request.

REFERENCES

[1] L. Schmitz, E. Ruskov, B. H. Deng, H. Gota, D. Gupta, M. Tuszewski, J. Douglass, W. A. Peebles, M. Binderbauer, and T. Tajima, "Multi-channel doppler backscattering measurements in the C-2 field reversed configuration," Rev. Sci. Instrum. **85**(11), 11D840 (2014).

[2] L. Schmitz, D. P. Fulton, E. Ruskov, C. Lau, B. H. Deng, T. Tajima, M. W. Binderbauer, I. Holod, Z. Lin, H. Gota *et al.*, "Suppressed ion-scale turbulence in a hot high-β plasma," Nat. Commun. **7**, 13860 (2016).

[3] I. Holod, W. L. Zhang, Y. Xiao, and Z. Lin, "Electromagnetic formulation of global gyrokinetic particle simulation in toroidal geometry," Phys. Plasmas **16**(12), 122307 (2009).

[4] D. P. Fulton, C. K. Lau, I. Holod, Z. Lin, and S. Dettrick, "Gyrokinetic particle simulation of a field reversed configuration," Phys. Plasmas (1994-present) **23**(1), 012509 (2016).

[5] D. P. Fulton, C. K. Lau, L. Schmitz, I. Holod, Z. Lin, T. Tajima, and M. W. Binderbauer, and TAE Team, "Gyrokinetic simulation of driftwave instability in field-reversed configuration," Phys. Plasmas **23**(5), 056111 (2016).

[6] C. K. Lau, D. P. Fulton, I. Holod, Z. Lin, M. Binderbauer, T. Tajima, and L. Schmitz, "Drift-wave stability in the field-reversed configuration," Phys. Plasmas **24**(8), 082512 (2017).

[7] C. K. Lau, "Electrostatic turbulence and transport in the field-reversed configuration," Ph.D. thesis (UC, Irvine, 2017).

[8] C. K. Lau, D. P. Fulton, J. Bao, Z. Lin, T. Tajima, L. Schmitz, S. Dettrick, and TAE Team, "Cross-separatrix simulations of turbulent transport in the field-reversed configuration," Nucl. Fusion **59**(6), 066018 (2019).

[9] J. Bao, C. K. Lau, Z. Lin, H. Y. Wang, D. P. Fulton, S. Dettrick, and T. Tajima, "Global simulation of ion temperature gradient instabilities in a field-reversed configuration," Phys. Plasmas **26**(4), 042506 (2019).

[10] Y. Hayakawa, T. Takahashi, and Y. Kondoh, "Classification of particle orbits and related stochasticity of plasma ion motion in a field-reversed configuration with d-3he advanced fuel," Nucl. Fusion **42**(9), 1075 (2002).

[11] L. Galeotti, D. C. Barnes, F. Ceccherini, and F. Pegoraro, "Plasma equilibria with multiple ion species: Equations and algorithm," Phys. Plasmas (1994-present) **18**(8), 082509 (2011).

[12] R. H. Cohen, A. Friedman, D. P. Grote, and J.-L. Vay, "Large-timestep mover for particle simulations of arbitrarily magnetized species," Nucl. Instrum. Methods Phys. Res., Sect. A **577**(1–2), 52–57 (2007).

[13] T. Tajima, "Computational plasma physics. with applications to fusion and astrophysics," Front. Phys. **72**, 1 (1989).

[14] T. Tajima and F. Perkins, in Proceedings of the Sherwood Theory Conference, 1983.

[15] A. Y. Aydemir, "A unified monte carlo interpretation of particle simulations and applications to non-neutral plasmas," Phys. Plasmas **1**(4), 822–831 (1994).

[16] Z. Lin, W. M. Tang, and W. W. Lee, "Gyrokinetic particle simulation of neoclassical transport," Phys. Plasmas **2**(8), 2975–2988 (1995).

[17] Y. Xiao, I. Holod, Z. X. Wang, Z. Lin, and T. Zhang, "Gyrokinetic particle simulation of microturbulence for general magnetic geometry and experimental profiles," Phys. Plasmas **22**(2), 022516 (2015).

[18] F. F. Chen, *Introduction to Plasma Physics and Controlled Fusion* (Springer, 1984), Vol. 1.

[19] Z. Gao, H. Sanuki, K. Itoh, and J. Q. Dong, "Temperature gradient driven short wavelength modes in sheared slab plasmas," Phys. Plasmas **10**(7), 2831–2839 (2003).

[20] Z. Gao, H. Sanuki, K. Itoh, and J. Q. Dong, "Short wavelength ion temperature gradient instability in toroidal plasmas," Phys. Plasmas **12**(2), 022502 (2005).

[21] J. Chowdhury, R. Ganesh, J. Vaclavik, S. Brunner, L. Villard, and P. Angelino, "Short wavelength ion temperature gradient mode and coupling with trapped electrons," Phys. Plasmas **16**(8), 082511 (2009).

[22] M. W. Binderbauer, T. Tajima, L. C. Steinhauer, E. Garate, M. Tuszewski, L. Schmitz, H. Y. Guo, A. Smirnov, H. Gota, D. Barnes, B. H. Deng, M. C. Thompson, E. Trask, X. Yang, S. Putvinski, N. Rostoker, R. Andow, S. Aefsky, N. Bolte, D. Q. Bui, F. Ceccherini, R. Clary, A. H. Cheung, K. D. Conroy, S. A. Dettrick, J. D. Douglass, P. Feng, L. Galeotti, F. Giammanco, E. Granstedt, D. Gupta, S. Gupta, A. A. Ivanov, J. S. Kinley, K. Knapp, S. Korepanov, M. Hollins, R. Magee, R. Mendoza, Y. Mok, A. Necas, S. Primavera, M. Onofri, D. Osin, N. Rath, T. Roche, J. Romero, J. H. Schroeder, L. Sevier, A. Sibley, Y. Song, A. D. Van Drie, J. K. Walters, W. Waggoner, P. Yushmanov, K. Zhai, and TAE Team, "A high performance field-reversed configuration," Phys. Plasmas **22**(5), 056110 (2015).

[23] H. Gota, M. W. Binderbauer, T. Tajima, S. Putvinski, M. Tuszewski, B. H. Deng, S. A. Dettrick, D. K. Gupta, S. Korepanov, R. M. Magee *et al.*, "Formation of hot, stable, long-lived field-reversed configuration plasmas on the c-2w device," Nucl. Fusion **59**(11), 112009 (2019).